Numerical Comparisons Between URANS and Hybrid RANS/LES at a High Reynolds Number Flow Using Unstructured Meshes

Ju-Yeol You* and Oh Joon Kwon**

Department of Aerospace Engineering, KAIST, Daejeon, 305-701, Korea

Abstract

In the present study, the turbulent flow fields around a circular cylinder at Re=3.6 x 10^6 were investigated based on an unstructured mesh technique, and the comparisons between URANS(S-A, SST) and hybrid RANS/LES(DES, SAS) methods for the simulation of high Reynolds number flow have been conducted. For this purpose, unsteady characteristics of vortex shedding and time-averaged quantities were compared. A quasi-steady solution-adaptive mesh refinement was also made for the URANS and hybrid RANS/LES approaches. The results showed that the simple changes in the turbulent length scale or source term of turbulent models made the flow fields less dissipative and more realistic in hybrid RANS/LES methods than the URANS approaches.

Key Words : Hybrid RANS/LES, URANS, Solution-adaptive mesh refinement, Unstructured meshes

Introduction

The flow fields around bluff bodies are of great interest to a wide range of engineering applications. Therefore flow around bluff bodies has been studied by many researchers through CFD[1-3] and experimental investigations[4,5]. A circular cylinder is one of the typical configurations of bluff bodies. The physics of flow around a circular cylinder is very complex. At high Reynolds number, the flow pattern is asymmetric and shows vortex shedding in the wake region. Additionally, the flow contains different scales of turbulent structures, which are called eddies. To capture these eddy structures, various methods of turbulent simulation such as URANS, LES, hybrid RANS/LES and DNS have been previously used. DNS and LES can provide time accurate turbulent dynamics, but they require very large computational costs due to the fine grid resolution near the solid surface. Therefore they have not been applied to high Reynolds number flows in spite of the higher accuracy. For this reason, URANS has been used for investigating high Reynolds number flows for several decades. URANS does not require large computational resources, but has limitations for capturing the detailed time variation of fluctuating eddies properly. To solve the problems related to URANS, LES and DNS for the simulation of high Reynolds number flows, hybrid RANS/LES techniques, which is URANS near the solid surface and LES for the rest of the computational domain, have been developed.

In the present study, S-A and SST models were employed for the URANS approach, and DES and SAS techniques were employed for the hybrid RANS/LES approach. The flow fields around a circular cylinder at Re=3.6 x 10^6 have been simulated. Unstructured mesh technique was adopted to model the 3-D configuration easily and distribute dense cells forcibly and adaptively in the wake region.

 * Graduated Student
** Professor
   E-mail : ojkwon@kaist.ac.kr
   Tel : +82-42-350-3720   Fax : +82-42-350-3710

Numerical Description

Numerical methods

A vertex-centered finite-volume scheme and an unstructured mesh technique were adopted to discretize the computational domain. The inviscid fluxes were calculated by using 2nd-order Roe's FDS, and the viscous fluxes were computed based on central differencing. A dual time stepping method and the Gauss-Seidel iteration were used for unsteady time integration.

Turbulent models

S-A model [6]

$$\frac{D\bar{v}}{Dt} = c_{b1}[1 - f_{t2}]\bar{S}\bar{v} + \frac{1}{\sigma}[\nabla((v + \bar{v})\nabla\bar{v}) + c_{b2}(\nabla\bar{v})^2]$$
$$- [c_{w1}f_w - \frac{c_{b1}}{\kappa^2}f_{t2}](\frac{\bar{v}}{d})^2 + f_{t1}\Delta U^2 \tag{1}$$

The last term is the trip term and was neglected in the present study because the flow at Re $= 3.6 \times 10^6$ is fully turbulent.

DES [7]

Spalart modified the length scale in the destruction term of the S-A model to resolve the turbulent structures properly.

$$d = \min(d, C_{DES}\Delta)$$
$$C_{DES} = 0.65, \quad \Delta = \max(\Delta x, \Delta y, \Delta z) \tag{2}$$

SST [8]

Menter combined the k-ω and k-ε equations in the form of k-ω equations.

$$\frac{\partial}{\partial t}\begin{bmatrix} \rho k \\ \rho w \end{bmatrix} + \frac{\partial}{\partial x_j}\begin{bmatrix} \rho u_j k \\ \rho u_j w \end{bmatrix} - \frac{\partial}{\partial x_j}\begin{bmatrix} (\mu_l + \sigma_k\mu_t)\frac{\partial k}{\partial x_j} \\ (\mu_l + \sigma_w\mu_t)\frac{\partial w^*}{\partial x_j^*} \end{bmatrix}$$
$$= \begin{bmatrix} \tau_{ij}\frac{\partial u_i}{\partial x_j} - \beta'\rho k w \\ \frac{\alpha}{v_t}\tau_{ij}\frac{\partial u_i}{\partial x_j} - \beta\rho w^2 + 2(1 - f_1)\frac{\rho\sigma_{w2}}{w}\frac{\partial k}{\partial x_j}\frac{\partial w}{\partial x_j} \end{bmatrix} \tag{3}$$

The last term of the ω-equation is the cross diffusion term from the combination of k-ω and k-ε.

SAS [9]

To resolve turbulent structures in unsteady regions, an additional term was added to the source term of the ω-equation in the SST model. Eq. (4) is the original form of SAS and Eq. (5) is the modified form to provide proper damping at the high wave number end of spectrum. In the present study, SAS 1 means the SAS with Eq. (4), and SAS 2 represents the form in Eq. (5).

$$Q_{SAS} = \rho F_{SAS}\max[\zeta_2\kappa S^2\frac{L}{L_{vK}} - \frac{2k}{\sigma_\phi}\max(\frac{|\nabla w|^2}{w^2}, \frac{|\nabla k|^2}{k^2}), 0]$$
$$L = \frac{\sqrt{k}}{C_\mu^{0.25}w}, \quad L_{vK} = \frac{\kappa S}{|\nabla^2 U|} \tag{4}$$

$$Q_{SAS} = \rho F_{SAS}\max[\zeta_2\kappa S^2(\frac{L}{L_{vK}})^2 - \frac{2k}{\sigma_\phi}\max(\frac{|\nabla w|^2}{w^2}, \frac{|\nabla k|^2}{k^2}), 0]$$
$$L = \frac{\sqrt{k}}{C_\mu^{0.25}w}, \quad L_{vK} = \max(\frac{\kappa S}{|\nabla^2 U|}, C_s\sqrt{\kappa\zeta_2 / ((\beta / c_\mu) - \alpha)}\Box\Delta) \tag{5}$$

Inflow and boundary conditions

S-A model and DES

$\bar{v}_\infty = 0.1v_\infty$ was applied at the inflow boundary, and $\bar{v} = 0$ was set on the solid surface.

SST model and SAS

$w_\infty = 10U_\infty / L$, $k_\infty = 0.1U_\infty^2 / \mathrm{Re}_L$ were applied at the inflow boundary, and $w_\infty = 60v / \beta\Delta d_1^2$, $k_\infty = 0$ were set on the solid surface.

Results and Discussion

Unstructured meshes

To discretize the computational domain, 7,586,758 cells, 1,635,230 nodes and 96,652 boundary faces were used as shown in Fig. 1. The initial thickness of the cell was $Y_1 = 10^{-5}$ D and stretched at $\Delta n+1/\Delta n = 1.25$ for 30 layers inside the boundary layer. To capture the turbulent structures in the detached wake region, dense cells, which were 6% of the diameter of the cylinder, were distributed.
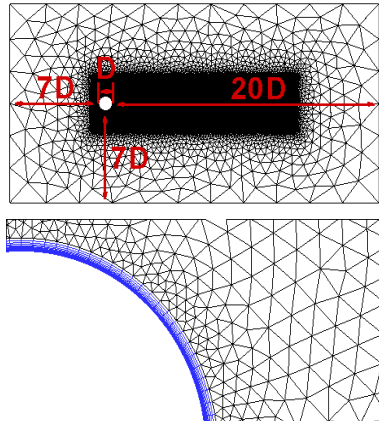
Fig. 1. Computational domain and
unstructured meshes

Unsteady characteristics

For unsteady simulations, a non−dimensional time step $tU_\infty / D = 0.002$ was used. Flow around the circular cylinder of Re=3.6×10^6 showed vortex shedding as in Fig. 2. URANS provided two−dimensional and regular vortex shedding, but hybrid RANS/LES provided three−dimensional and irregular one. From Fig. 2, the URANS approach is more dissipative than hybrid RANS/LES. Actually, the eddy viscosity ratio at the symmetric plane in Fig. 3 shows that the URANS approach gives larger eddy viscosity than hybrid RANS/LES, and so prevented generating the 3−dimensional structure. For the SAS approach, SAS 2 was more dissipative than SAS 1 because SAS 2 was modified to provide more damping with the wave number of mesh size. For URANS approaches, SST model was more dissipative than S−A model. In Fig. 4, the Strauhal numbers of each case were 0.25 that was well matched with the experimental data of St = 0.27[4].
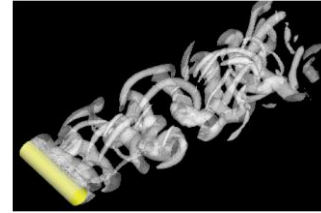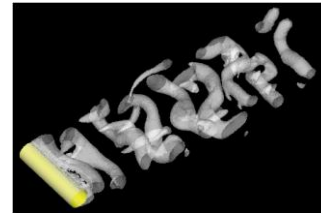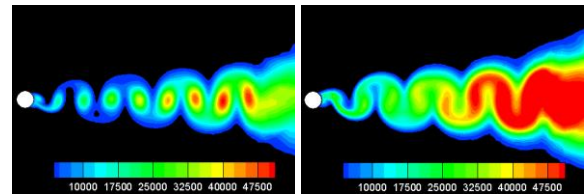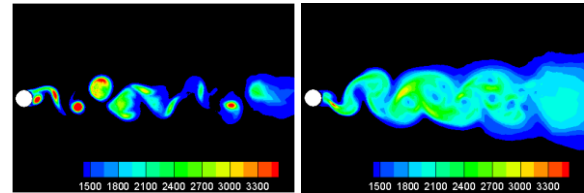

(a) S−A
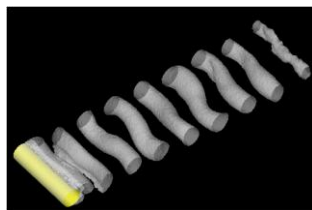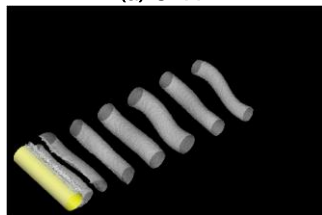
(b) SST
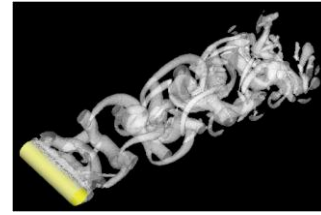
(c) DES

(d) SAS 1

(e) SAS 2

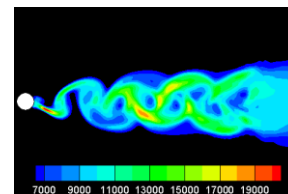Fig. 2. Instantaneous iso−surfaces of S2−Ω2

(a) S−A   (b) SST

(c) DES   (d) SAS 1

(e) SAS 2

Fig. 3. Instantaneous eddy viscosity ratio(μ_t / μ) at the symmetric plane
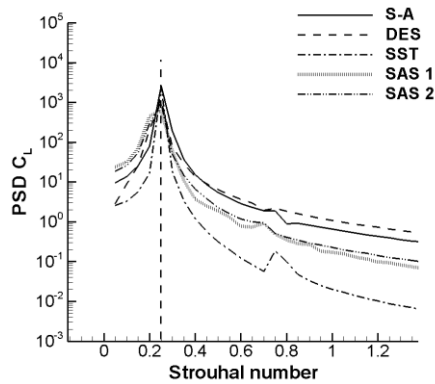
Fig. 4. Power spectrum density of lift coefficient

Time-averaged quantities

Unsteady simulation was conducted for 40 non−dimensional time and was averaged from 20 non−dimensional time. The pressure coefficient, averaged with time and spanwise direction, on the surface of the cylinder is shown in Fig. 5. The negative peaks of the present calculations were smaller than the experiment[5] and other researcher's result[9]. This may be caused by the lack of the number of points in the circumstantial direction of the cylinder. This tendency was more magnified in the hybrid RANS/LES approaches because the momentum transfer of the hybrid RANS/LES was smaller than that of URANS due to smaller eddy viscosity.

In Fig. 6, the time−averaged velocity vectors at the symmetric plane are presented. The recirculation bubbles can be observed, and the size of the recirculation bubbles of hybrid RANS/LES was slightly larger than URANS.
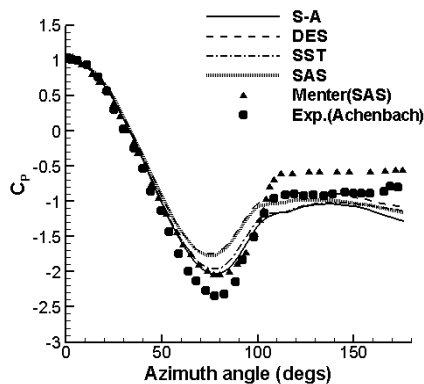

Fig. 5. Pressure coefficient distribution on the surface of circular cylinder
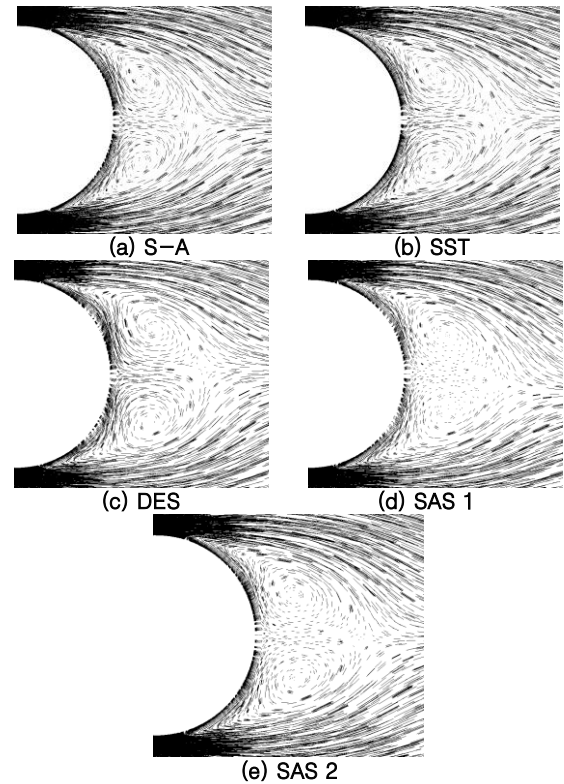

Fig. 6. Time−averaged velocity vectors at the symmetric plane

Additionally, the magnitude of recirculation was larger for hybrid RANS/LES. These can also be confirmed in Fig. 7. In Fig. 7, the first figure shows that the magnitude of the flow reversal in the recirculation zone is larger with hybrid RANS/LES approaches than with URANS methods. After the recirculation, the time−averaged streamwise velocity was recovered slower with hybrid RANS/LES than with URANS as seen on the second figure because of the strong irregularity of the flow fields with hybrid RANS/LES.

In Fig. 8, it is shown that the time−averaged turbulent kinetic energy $(<u'u'>+<v'v'>+<w'w'>)/U_\infty^2$ becomes larger on the streamwise centerline than surroundings. Table. 1 shows the location of the maximum turbulent kinetic energy for each approach. Hybrid RANS/LES provided a slightly larger magnitude of the turbulent kinetic energy and the location of the maximum value of them is at further downstream than that of URANS.

From Fig. 9, it is shown that the time−averaged turbulent kinetic energy was dominated by the transverse component $<w'w'>/U_\infty^2$.

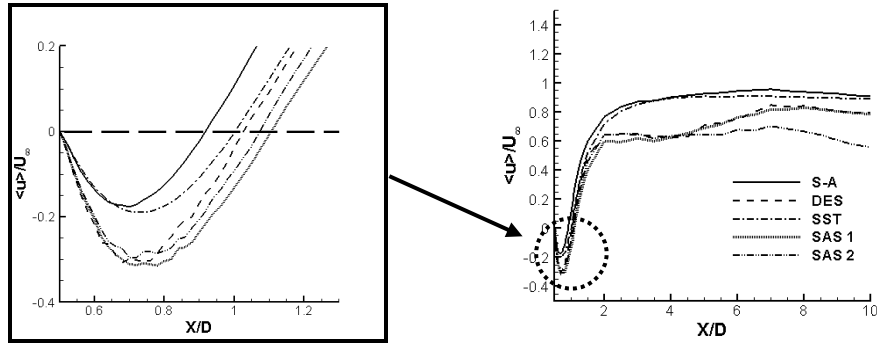Fig. 7. Time-averaged streamwise velocity
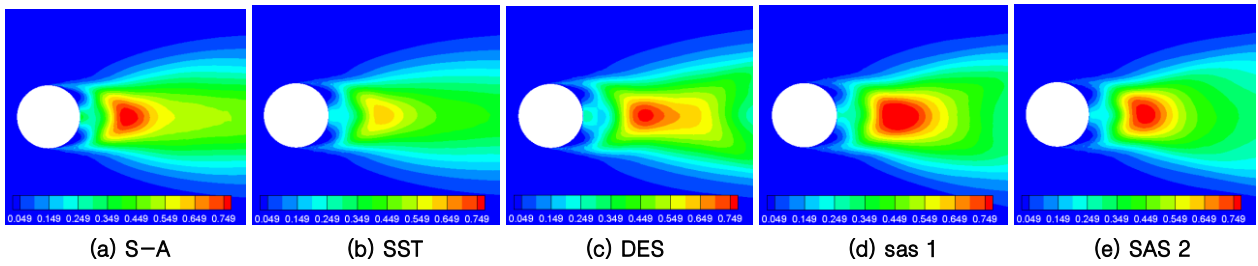
Fig. 8. Time-averaged turbulent kinetic energy at the symmetric plane

(a) S-A   (b) SST   (c) DES   (d) sas 1   (e) SAS 2
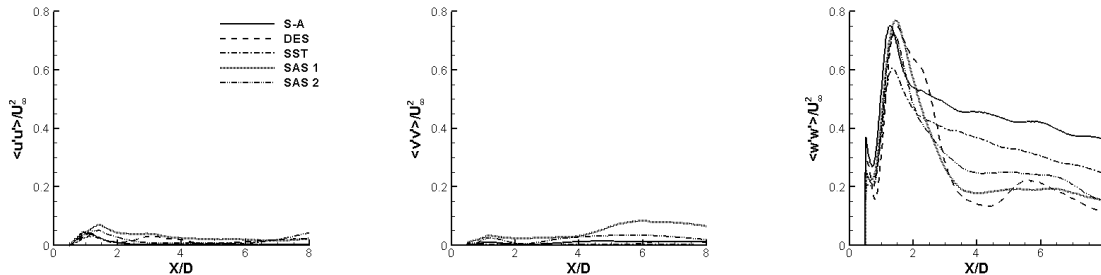
Fig. 9. Time-averaged Reynolds normal stress distribution along the streamwise centerline
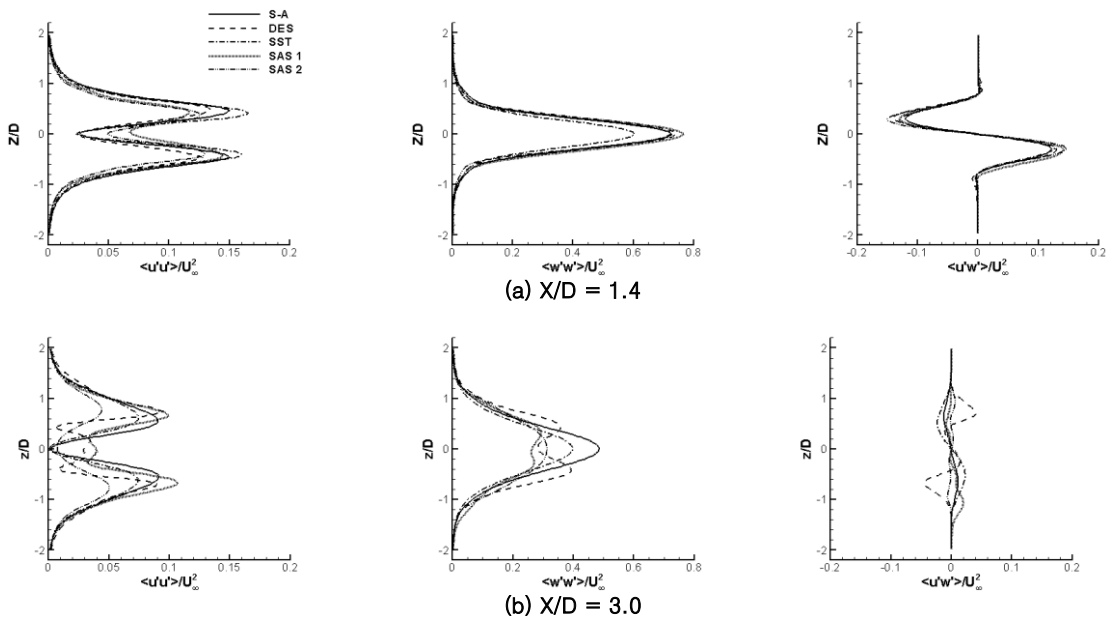
(a) X/D = 1.4

(b) X/D = 3.0

Fig. 10. Time-averaged Reynolds stress distribution on the transverse symmetric line

Table 1. Location of maximum turbulent kinetic energy

	S-A	DES	SST	SAS 1	SAS 2
X/D	1.251	1.444	1.318	1.446	1.401

Fig. 10 shows the Reynolds normal stress in the streamwise direction $<u'u'>/U_\infty^2$, the Reynolds normal stress in the transverse direction $<w'w'>/U_\infty^2$, and the Reynolds shear stress $<u'w'>/U_\infty^2$ at different downstream locations X/D = 1.4 and X/D = 3.0. The streamwise normal stresses were smaller at the centerline than surroundings. At the downstream, the peaks were flattened. The streamwise normal stresses approach zero faster with URANS. It means that the turbulent fluctuation in the streamwise direction of URANS was dissipated faster than hybrid RANS/LES. The maximum peak of the transverse normal stress was at the centerline near the cylinder, but the peak moved out of the centerline at downstream due to the irregular vortex shedding for hybrid RANS/LES. The shear stresses were skew symmetric near the cylinder, and made zero contribution with the reversal of sign at the wake centerline. This change of sign was due to the conservation of angular momentum across the centerline. Further downstream, the shear stresses were also reduced to zero.

Solution-adaptive mesh refinement

The quasi-steady solution-adaptive mesh refinement technique has been applied to reduce the computational costs of simulation of the URANS and hybrid RANS/LES approaches. S-A model was used for the URANS approach and DES was used for the hybrid RANS/LES approach. The vorticity was used as the criterion to define the regions where the refinement would be necessary.

(a) Initial mesh   (b) First-refined mesh   (c) Second-refined mesh
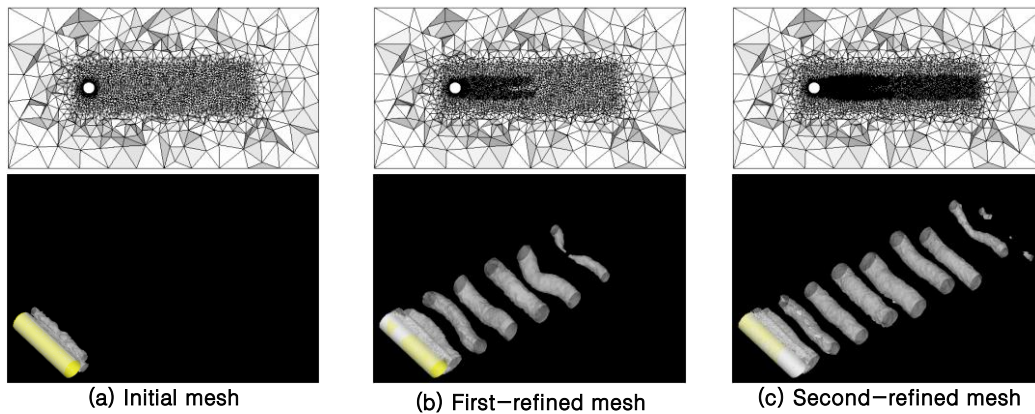
Fig. 11. Refined mesh and instantaneous iso-surfaces of $S^2-\Omega^2$ with S-A model

(a) Initial mesh   (b) First-refined mesh   (c) Second-refined mesh
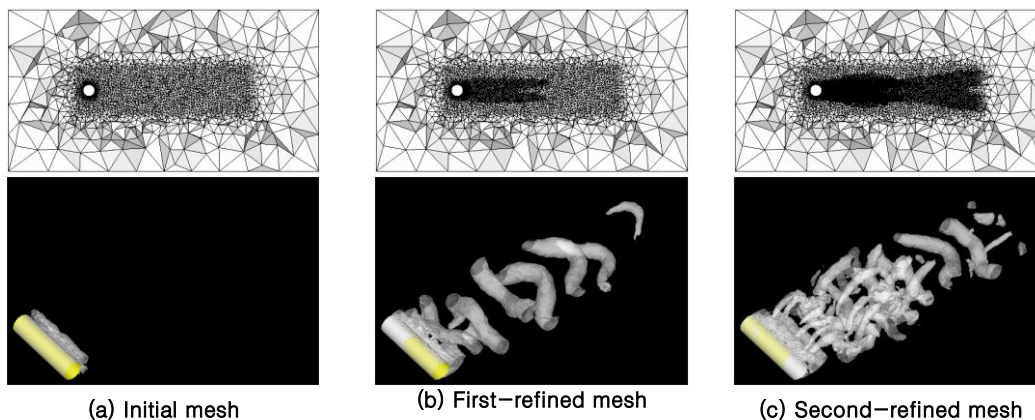
Fig. 12. Refined mesh and instantaneous iso-surfaces of $S^2-\Omega^2$ with DES approach

Table 2. The number of cells and nodes for each refinement step

	S−A		DES
Initial mesh	640,287cells, 193,358 nodes		
First−refined mesh	2,010,254 cells, 696,9291 nodes	First−refined mesh	2,054,487 cells, 676,835 nodes
Second− refined mesh	4,052,538 cells, 1,015,641 nodes	Second− refined mesh	4,565,683 cells, 1,102,190 nodes

Table. 2 shows the number of cells and nodes for each refinement step. Fig. 11 and Fig. 12 show the results of the mesh refinement. Due to the irregular vortex shedding, the refined region of the hybrid RANS/LES approach was broader than that of the URANS approach. As the refinement proceeds, the shedding pattern was also changed more dramatically in the hybrid RANS/LES approach than the URANS simulation. Fig. 13 shows the pressure coefficient, averaged with time and spanwise direction, on the surface of the cylinder. With the URANS technique, the pressure coefficient was converged on the second−refined mesh. However it was changed according to the refinement procedure with the hybrid RANS/LES approach.

Fig. 13. Pressure coefficient distribution on the surface of circular cylinder

Conclusion

In the present study, URANS and hybrid RANS/LES approaches based on an unstructured mesh technique have been developed and applied to simulate the flow fields around a circular cylinder at Re = 3.6×10^6. With hybrid RANS/LES methods, the vortex shedding was more irregular than with URANS method and showed three−dimensional patterns. The Strouhal number was 0.25 for every case. The pressure distribution on the cylinder under− predicted the peak value for every case, but after the separation the present calculations were well matched with experimental data. The recirculation bubble size behind the cylinder was larger with hybrid RANS/LES than with URANS. The time−averaged turbulent kinetic energy was dominated by transverse fluctuation and the maximum values were higher for hybrid RANS/LES. The locations of the maximum turbulent kinetic energy were further downstream for hybrid RANS/LES. The streamwise normal stress showed higher peak with URANS, but dissipated faster than hybrid RANS/LES. Near the circular cylinder, the transverse normal stress had the maximum value at the centerline for URANS and hybrid RANS/LES. However, further downstream, the magnitude of the transverse normal stress at the centerline was smaller than surroundings for hybrid RANS/LES due to the irregular fluctuation of the shedding vortex.

The results showed the URANS approaches are more dissipative and show more regular flow field than hybrid RANS/LES. Similar patterns were also observed for the solution− adaptive mesh refinement cases. All differences between URANS and hybrid RANS/LES approaches were resulted from the simple
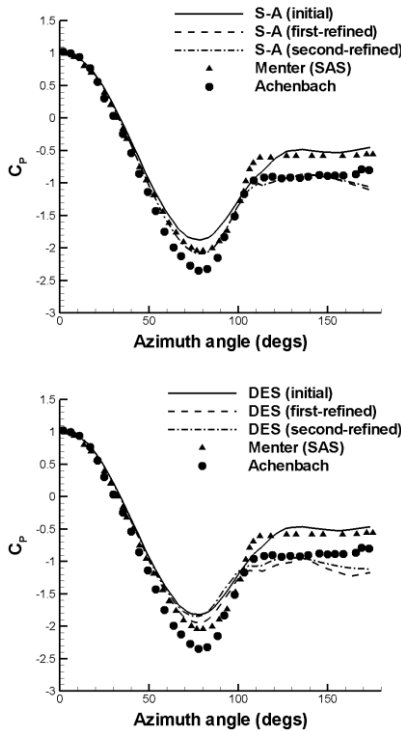
changes in the turbulent length scale or source term of turbulent models. These changes made flow fields less dissipative and more realistic in the hybrid RANS/LES methods by activating the destruction term(DES) or increasing the specific dissipation rate(SAS).

Acknowledgements

References

1. Nichols, R.H., 2005, "Comparison of Hybrid RANS/LES Turbulence Models on a Circular Cylinder at High Reynolds Number", 43rd AIAA Aerospace Science Meeting and Exhibit, Reno, AIAA 2005-498.

2. Krishnan, V. and Squires, K.D., 2006, "Prediction of the Flow around a Circular Cylinder at High Reynolds Number", 44th AIAA Aerospace Science Meeting and Exhibit, Reno, AIAA 2006-901.

3. Ong, M.C., Utnes, T., Holmedal, L.E., Myrhaug, D. and Pettersen, B., 2009, "Numerical Simulation of Flow around a Smooth Circular Cylinder at Very High Reynolds Numbers", Marine Structures, Vol.22, pp. 142-153.

4. ROSHKO, A., 1961, "Experiments of the Flow Past a Circular Cylinder at Very High Reynolds Number", J. Fluid Mechanics, Vol.10, pp. 345-356.

5. ACHENBACH, M., 1968, "Distribution of Local Pressure and Skin Friction around a Circular Cylinder in Cross-Flow up to Re=5×10^6," J. Fluid Mechanics, Vol.34, pp. 625-639.

6. Spalart, P.R. and Allmaras, S.R., 1992, "A One-Equation Turbulence Model for Aerodynamic Flows", 30th AIAA Aerospace Science Meeting and Exhibit, Reno, AIAA 1992-0439.

7. Spalart, P.R, 2001, "Young-Person's Guide to Detached-Eddy Simulation Grids," NASA CR-2001-211032.

8. Menter, F.R., 1994, "Two-Equation Eddy Viscosity Turbulence Models for Engineering Applications", AIAA J., Vol.32, pp. 1598-1605.

9. Menter, F.R. and Egorov, Y., 2005, "A Scale-Adaptive Simulation Model using Two-Equation Models", 43rd AIAA Aerospace Science Meeting and Exhibit, Reno, AIAA 2005-1095.